Molecular dynamics of interfacial crystallization of dodecane on hydroxylated silica surface impacted by H_2O and CO_2

C. Chen ⓘ ; J. Xia ✉ ⓘ ; Q. Martinez ⓘ ; X. Jiang ⓘ ; H. Bahai ⓘ

Check for updates

View Online

Export Citation

CrossMark

Articles You May Be Interested In

The dynamics of titanium ethoxide-doped dodecane droplet microencapsulation

Journal of Applied Physics (September 1988)

Effects of the surroundings and conformerisation of *n*-dodecane molecules on evaporation/condensation processes

J. Chem. Phys. (January 2015)

A molecular dynamics study of local pressures and interfacial tensions of SDS micelles and dodecane droplets in water

J. Chem. Phys. (June 2016)

AIP Publishing

Molecular dynamics of interfacial crystallization of dodecane on hydroxylated silica surface impacted by H₂O and CO₂

View Online   Export Citation   CrossMark

C. Chen,[1] J. Xia,[1,a] Q. Martinez,[1] X. Jiang,[2] and H. Bahai[1]

AFFILIATIONS

[1] Department of Mechanical and Aerospace Engineering, Brunel University London, Uxbridge UB8 3PH, United Kingdom
[2] School of Engineering and Materials Science, Queen Mary, University of London, London E1 4NS, United Kingdom

[a] Author to whom correspondence should be addressed: jun.xia@brunel.ac.uk

ABSTRACT

The morphology of dodecane in a nanopore at temperatures typical in exploited or depleted oil reservoirs is investigated using molecular dynamics simulation. The dodecane morphology is found to be determined by interactions between interfacial crystallization and surface wetting of the simplified oil, while "evaporation" only plays a minor role. The morphology changes from an isolated, solidified dodecane droplet to a film with orderly lamellae structures remaining within, and finally to a film containing randomly distributed dodecane molecules, as the system temperature increases. In a nanoslit under the impact of water, since water wins against oil in surface wetting on the silica surface due to electrostatic interaction induced hydrogen bonding between water and the silanol group of silica, the spreading of dodecane molecules over the silica surface is impeded by this water confinement mechanism. Meanwhile, interfacial crystallization is enhanced, leading to always an isolated dodecane "droplet," with crystallization weakening as the temperature increases. Since dodecane is immiscible to water, there is no mechanism for dodecane to escape the silica surface, and the competition of surface wetting between water and oil determines the morphology of the crystallized dodecane droplet. For the CO₂–dodecane system in a nanoslit, CO₂ is an efficient solvent for dodecane at all temperatures. Therefore, interfacial crystallization rapidly disappears. The competition of surface adsorption between CO₂ and dodecane is secondary for all cases. The dissolution mechanism is a clear clue for the fact that CO₂ is more effective than water flooding in oil recovery for a depleted oil reservoir.

I. INTRODUCTION

CO₂ capture, utilization, and storage is one of the most promising decarbonization technologies to achieve green industrial growth and address the challenge of global climate change. By injecting captured CO₂ into existing oil reservoirs, it is possible to simultaneously achieve CO₂ geo-sequestration and oil recovery (CO₂-EOR). Under typical undersurface conditions, supercritical CO₂ has properties between liquid and gas, such as high diffusivity, low viscosity, and vanishing surface tension, which implies that CO₂ enhanced oil recovery is different from the secondary oil recovery via water flooding. It is an established engineering practice to use the tertiary CO₂-EOR following the secondary water flooding,[1] but the scientific understanding of the mechanisms behind the fact that

CO₂-EOR is superior to water flooded EOR for an exploited or depleted oil reservoir remains to be improved to better guide and optimize CO₂-EOR.

The undersurface geological formation features nanoporous media, containing inorganic caprock in circular, angular, slit shape on the scale of 10–50 nm.[2] The nano-confined fluids, such as CO₂, water, and oil, can possess peculiar transport properties that deviate from those on bulk scale. For example, functional groups on solid surface determine its wettability, which affects the slip length of water.[3–6] The pore size, wettability, and nano-confinement effects can significantly affect the minimum miscibility pressure of CO₂/oil.[7–9] Supercritical fluids in nano-pores not only exhibit anomalous diffusion, featuring trapping on solid surface, random hopping and desorption,[10,11] but also have a shift of thermody-

namics properties, such as the vapor–liquid coexistence curve and pseudo-boiling lines.[12,13] Moreover, previous studies reported the existence of immobile solid-like crude oil on caprock surfaces due to adsorption, named as "sticky layers."[14–20] The injected CO_2 can reduce both the sticky layer thickness and hydrocarbon viscosity, thereby enhancing the flow of oil.[20,21] It is clear that detailed quantitative information on the molecular conformation on caprock is of great importance for better understanding the flow and transport dynamics of the nano-confined oil in CO_2-EOR processes. To the best of our knowledge, however, there have been few studies on investigating oil solidification/crystallization on rock surfaces, much less accurate predictions of the layering structures of oil stacks attached on the surfaces, especially under the impact of H_2O and CO_2 during water flooding and CO_2 injection.

Crude oil is a mixture of paraffin/n-alkanes of high molecular weights with the general formula of C_nH_{2n+2}, e.g., isoalkanes, naphthenes, aromatics asphaltenes. It is believed that the crystallization of alkanes at low temperature and the subsequent aggregation, perception, and gelation are the primary reasons for the wax deposition.[22,23] Waxy crude oil is a long-standing concern for petroleum industry, especially in offshore reservoir development, crude oil exploitation and transportation where the ambient temperature is always unfavorably below the cloud point temperature of oil. Crystallization of alkanes occurs much more easily on an attractive solid substrate with moderate supercooling.[24–26] More comparable phenomena, such as the nematic-to-crystal transition of polymer films on a crystal slab,[27,28] epitaxial crystal growth of alkanes,[29,30] self-crystallization/surface freezing of n-alkanes on the surface of SiO_2 nanoparticles,[31,32] and the elusive layering structure transition of hydrocarbon lubricant in nanoslit,[33–37] indeed indicate that the interfacial crystallization of oil on caprock surfaces is ubiquitous.

Modeling and comparing water flooded and CO_2-EOR is challenging when interfacial crystallization of oil needs to be taken into account because (1) components can be in gas, liquid, or solid phases (more accurately, a ternary-phase mixture as we will see from simulation results reported herein) under supercritical conditions; (2) phase transitions are likely to occur and interact at the interface; (3) transport properties can be peculiar due to the nanoconfinement. Molecular dynamics (MD) simulation has proven to be a proper and useful tool to reveal the mechanisms of microscopic phase transition dynamics, such as alkane melting,[38] and to accurately predict the transport properties of alkanes over a wide range of conditions.[39] The application of MD simulation in oil recovery was reviewed by Ahmadi and Chen[14] under the conditions of 298–373 K and 15–35 MPa, where the oil is approximated by either one species or a mixture of alkanes (decane, octane, decane, and dodecane), aromatics, asphaltene, etc., and the caprock by quartz, hydroxylated silica, kaolinite, carbonate, etc. MD simulation has also been used widely for studying the effects of nano-confinement on CO_2 enhanced shale-gas recovery, as reviewed in the work of Yu et al.[2] and Wang et al.[40]

In this study, three systems were inspected, i.e., dodecane–silica (System 1—S1), silica–H_2O–dodecane–silica (System 2—S2) and silica–CO_2–dodecane–silica (System 3—S3). Dodecane and hydroxylated silica are used to approximate oil and caprock, respectively. MD simulation is performed to first investigate and better understand the interfacial crystallization of oil on caprock surface in S1
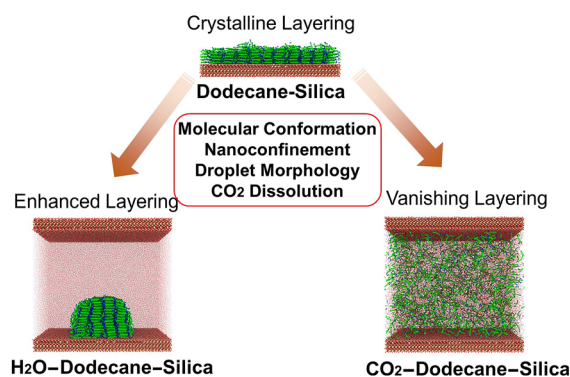

FIG. 1. Interfacial crystallization under the impact of H_2O and CO_2.

at 310–410 K, which covers typical reservoir temperatures.[41,42] With a detailed, quantified understanding obtained of the oil morphology that is typical in exploited or depleted oil reservoirs, the effects of water (S2) and CO_2 (S3) on crystallized dodecane are studied and compared, mimicking simplified engineering operation of water flooding and CO_2 injection. Statistics on molecular conformation and dodecane morphology are obtained, investigated, and compared among the three systems.

The paper is organized as follows: The methodology of MD simulation is introduced in Sec. II, including the force field, system energy, molecular model and system configuration, with validation. Two different methods on pressure control are introduced and compared. Results and discussions are presented in Sec. III and summarized in Fig. 1, including temperature dependent interfacial crystallization on hydroxylated silica surface interacting with surface wetting in S1 in Sec. III A; in Sec. III B, water comes into play in S2 and affects the interfacial crystallization through winning surface wetting over dodecane through electrostatic interaction induced hydrogen bonding. In S3 in Sec. III C, supercritical CO_2 acts as an efficient solvent for dodecane and therefore dissolution dominates over interfacial crystallization, which vanishes quickly. Finally, the conclusions are summarized in Sec. IV.

II. METHODOLOGY AND MOLECULAR MODELING SETUP

A. Molecule model, force field, and system configuration

The molecular structures of silica, dodecane, H_2O, and CO_2 are shown in Fig. 2. Hydroxylated silica with surfaces terminated by 9.4 silanol groups (named as Q2 in the present study) per nm × nm is used to approximate the underground caprock. The interfacial force field (IFF) parameters developed in the work of Heinz et al.[43] are used for silica–Q2, which have been shown to be able to accurately predict interfacial properties, such as hydrogen bonding, surface adsorption, and the contact angle in CO_2–brine–silica systems.[44,45] The SPCE (extended simple point charge) model is used for water molecule. The TraPPE force field
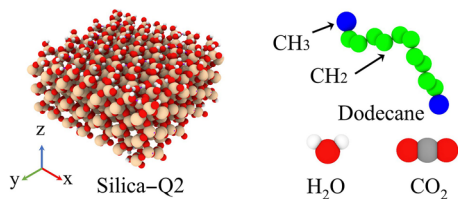
FIG. 2. Molecular structures of hydroxylated silica, dodecane, H_2O and CO_2. The Q2 unit cell is generated from the cleavage and hydration of the α-quartz (001) plane. The TraPPE force field of dodecane is the united-atom (UA) model, where the CH_3 and CH_2 groups are treated as single particles.

TABLE I. Number of CO_2 molecules in silica–CO_2-dodecane–silica system (S3) to keep the pressure at 20 MPa.

T (K)	310	330	350	370	390	410
N (10^3)	36	31	26	21	17	15

is used for dodecane molecule, which was developed by Potoff and Siepmann[46] for predicting vapor–liquid phase equilibria of CO_2 and alkane mixtures. The TraPPE force field can accurately predict the transport properties of alkanes, such as density, surface tension and critical points, over a wide range of conditions including super-critical regimes.[39,47] The energy functions of TraPPE and IFF are compatible with each other. The dihedral and improper energies are not considered for silica in the IFF force field.[43] The details of force fields and their key parameters are given in supplementary material.

Three systems are built, i.e., dodecane–silica (S1), silica–H_2O-dodecane–silica (S2), and silica–CO_2-dodecane–silica (S3), as shown in Fig. 3. All the systems have the same silica slab, which is generated by patterning the Q2 unit cell in x and y directions by 6 and 3 times, respectively, finally containing 33 264 atoms. The thickness of the silica slab is 1.88 nm. 1500 dodecane molecules are packed in rectangular box, which is placed on silica surface with a 0.2 nm gap. 100 000 H_2O water molecules are deployed in S2, while the number of CO_2 molecules in S3 varies according to the temperature, as shown in Table I, in order to keep the bottom layer of the upper silica slab at ~18.5 nm in z direction and the pressure at 20 MPa.
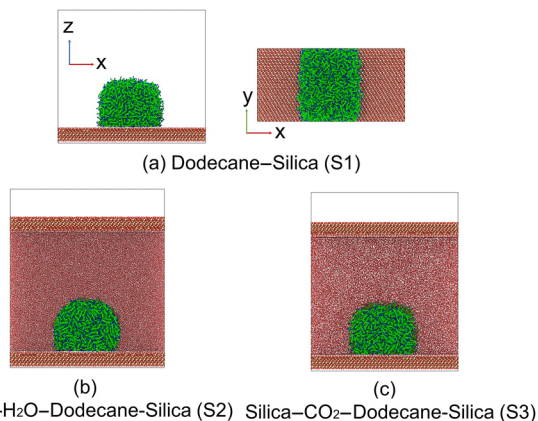

FIG. 3. Initial configurations of the systems: dodecane–silica (S1), silica–H_2O-dodecane–silica (S2) and silica–CO_2-dodecane–silica (S3); CO_2 and H_2O molecules are in vdW representation with a 0.5 scaling factor; the domain size of the dodecane–silica system (S1) is 20.87, 10.28, 18.50 nm in x, y, z directions, respectively.

B. MD setup

All simulations are performed using Large-scale Atomic/Molecular Massively Parallel Simulator (LAMMPS).[48] Post-processing and visualization are performed in OVITO (The Open Visualization Tool).[49] The time step in production run is 1 fs. The cut off distance for LJ interaction and Coulomb force is 1.2 nm. MD simulations with 1.4 nm as the cut off distance have also been performed, and there is no systematic difference in properties of dodecane in bulk phase, including densities and other molecular structure/distribution statistics (not shown), between the two setups for cut off distance. PPPM (particle–particle particle-mesh) is used for long-range Coulomb force in k-space with an accuracy of 10^{-5}. Periodic boundary conditions are used in x and y directions, while non-periodic fixed boundary conditions are used in z direction. A vacuum slab whose length is three times the domain length in z direction is inserted to virtually turn off atom interactions in this direction.

The non-periodic harmonic wall boundary is set in z direction, where the energy of wall-particle interactions is given by a harmonic spring potential: $E = \mu(r - r_c)^2$ $(r < r_c)$, where μ is the strength factor for wall-particle interaction, r is the distance from the particle to the wall, and r_c is the cut off distance at which the particle and wall no longer interact.

For uniform systems of the liquids in bulk phase, the NPT (N: number of atoms, P: pressure, T: temperature) and NVT (V: volume) ensembles are used to maintain the system size, temperature, and pressure. Generally, there are two methods to obtain the targeted pressure of the nano-confined "liquids," as shown in Fig. 4, either by applying additional forces (f_i) on a group of silica atoms to make them move like a piston[50,51] (method 1—M1) or by displacing the slab (method 2—M2) with a designed velocity until a certain position, thereby achieving an equivalent volume.[44,45,52] To avoid the overlap of atoms, liquid molecules are deployed with a slightly lower density than that of the liquid phase. The temperatures of CO_2, H_2O and dodecane are maintained by the Nose-Hoover thermostat,[53] while the temperature of silica is controlled by the Berendsen thermostat:[54] $f_i = PS/N$, where f_i is the force per atom. N is the number of atoms in the group (G5 in Fig. 4). P and S are the targeted pressure and the area of the slab in x–y plane, respectively.

C. Validation of molecular model/setup and uncertainties

The density of CO_2 predicted by the TraPPE force field shows excellent agreement with NIST data, while the deviation in H_2O increases with temperature, with 2.14% lower than NIST data at 410 K (see Fig. 1 in supplementary material). The capability of the TraPPE force field on predicting the density of dodecane has been justified in our previous studies,[39,55] with the averaged deviation
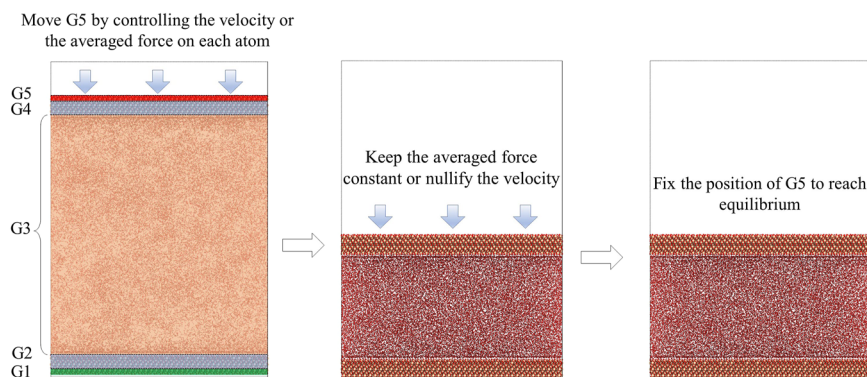
07 October 2023 12:30:18

FIG. 4. Schematic showing the temperature and pressure control in silica–liquid–silica system. G1 is a group of silica atoms to fix the position of the bottom slab, which is 0.45 nm in thickness and has 10 116 atoms; G2 is a group of the remaining silica atoms to control the temperature; G3 is the group of liquid atoms; G4 is a group of silica atoms to control the temperature using the same thermostat as for G2; G5 is a group of silica atoms to apply an extra force or control the velocity.

being ~1% as the temperature and pressure vary in 300–700 K and 1–1000 bar, respectively.

Figures 5(a) and 5(b) show the compression of liquid by controlling the forces uniformly on each atom in G5 in z direction in Method 1. The z-location of the center of mass (COM) of the upper silica slab in silica–H_2O–silica system decreases monotonously before 0.1 ns, followed by the convergence. At higher temperatures the COM z-locations converge more slowly and until after 0.5 ns. The COM of the upper silica slab in silica–CO_2–silica system shows much stronger oscillations, especially at higher temperatures above 350 K. Although controlling the pressure by adding forces works well for H_2O, the simulation takes a long time in systems contain-

ing CO_2 (longer than 10 ns at 410 K) to converge. Figure 5(c) shows the time evolution of the COM z-location of the upper slab and the number of CO_2 molecules adsorbed on the bottom slab surface by moving the upper slab with a constant velocity—Method 2. There are three stages, i.e., the upper slab is kept fixed while CO_2 is thermostated at the corresponding temperature in the initial 0.5 ns, then move it with a constant velocity for 1.0 ns to the targeted position, and finally fix the positions of G5 atoms until the system reaches an equilibrium. It can be seen from the time evolution of the number of CO_2 molecules adsorbed on the bottom slab, all systems converge easily after 1.5 ns, which is more efficient than M1 shown in Fig. 5(b). The density profiles of CO_2 at 2.5 ns in nano-confined
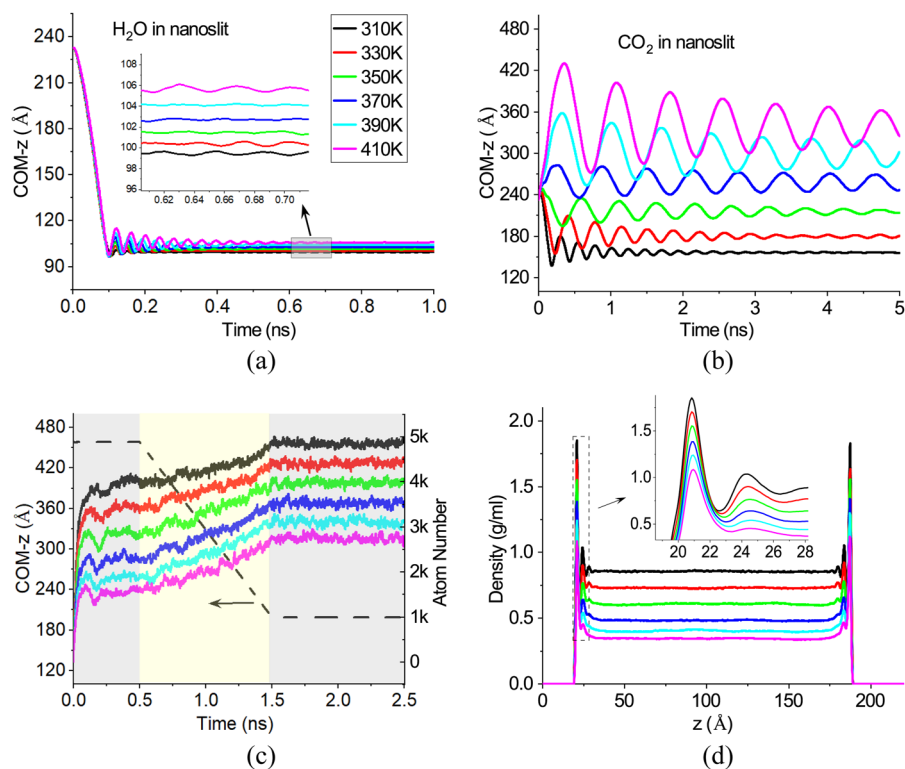

FIG. 5. Pressure control. (a) z-location of upper slab COM using M1 for H_2O. (b) z-location of upper slab COM using M1 for CO_2. (c) z-location of upper slab COM using M2 for CO_2. (d) CO_2 density along z at 2.5 ns.

TABLE II. Statistics uncertainty: relative standard deviation σ on five independent cases for each system S1, S2 and S3 at 330 K.

σ (%)	S1	S2	S3
$\sigma_{\rho_{\text{peak,1}}}$ [a]	0.32	1.04	2.01
$\sigma_{\rho_{\text{peak,2}}}$	0.78	1.26	0.45
$\sigma_{\rho_{\text{peak,3}}}$	1.77	1.68	[b]
$\langle \sigma | \rho > 0.1\rho_{\text{max}} \rangle$ [c]	2.88	7.38	1.01

[a] $\rho_{\text{peak},i}$: peak density of the i-th adsorption layer of dodecane on silica surface.
[b] No distinct 3rd peak.
[c] The condition $\rho > 0.1\rho_{\text{max}}$ is to exclude regions where the molecule number is low.

direction is also obtained with a bin width of 0.1 Å in z direction, as shown in Fig. 5(d), where the density is reasonably higher in the adsorbed regions close to the slabs. Therefore, M1 and M2 will be used to control the pressure in S2 and S3, respectively.

To illustrate the uncertainty levels of the results obtained in this study, in addition to the case results and statistics reported later, we have also performed another four independent cases for each system S1, S2 and S3 at 330 K with different initial conditions for molecules. Table II presents, for the five independent cases, the relative standard deviations σ for the peak densities of the first three adsorption layers of dodecane on silica surface, together with the conditionally averaged σ over z direction of the dodecane density. The condition $\rho > 0.1\rho_{\text{max}}$ is to exclude regions where the molecule number is low.

III. RESULTS AND DISCUSSION

A. Dodecane–silica system (S1)

1. Dodecane morphology—interfacial crystallization vs surface wetting, with evaporation

The snapshots of the dodecane morphology at different times at 330 K and the layouts of the molecules attached to silica (the attached layer) at 310–410 K are shown in Fig. 6. The time evolution of the orientational order and structure properties of dodecane molecules quantified by the radial distribution function (RDF) and the probability distribution function (PDF) of the end-to-end distance is shown in Fig. 7. The corresponding values for dodecane in bulk phase are also obtained for comparison.

The orientational order parameter is defined as the averaged second-order Legendre polynomial of the angle between the molecular principal axis and the reference axis:[56,57] $P_{ee}(\theta) = \sum_{i=1}^{3} P_{ee}(\theta_i)$, and $P_{ee}(\theta_i) = (3\langle \cos^2\theta_i \rangle - 1)/2$, where θ is the angle between the dodecane end-to-end vector and the reference axis of x, y or z; $\langle \cdot \rangle$ is ensemble average. $P_{ee}(\theta_i) = 1$ when the end-to-end vector is parallel to the reference axis i.

The atomic RDF, i.e., $g(r)$, is a parameter describing the short-to-long-range order of materials on nanoscale. RDF is a measure of the probability of finding a particle at a distance of r away from a given reference particle. It varies significantly for solids, gases, and liquids, as the peak magnitudes would indicate. The RDF is defined as $g_{mn}(r) = dN_{mn}(r)/(4\pi\rho_n r^2 dr)$, where ρ_n is the number density of type-n particles in the system, and N_{mn} is the number of type-n particles distributing in the sphere of radius r with the center as particle m.
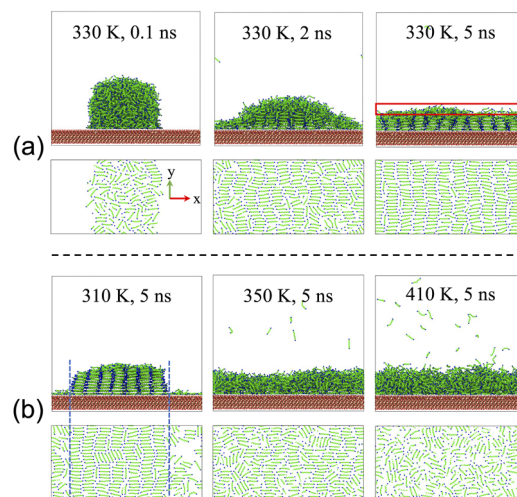

FIG. 6. (a) Time evolution of interfacial dodecane crystallization in S1 at 330 K and the corresponding dodecane layout of the contact monolayer. The free surface is highlighted in (330 K, 5 ns). (b) Snapshots of S1 and the attached layer at different temperatures at 5 ns. The droplet boundary is indicated by blue dashed lines in (310 K, 5 ns).

The temperature dependent morphology of dodecane in Fig. 6 is the result due to the collective dynamics of molecule spreading (surface wetting) over the substrate, interfacial crystallization, and evaporation.

The melting temperature of dodecane is ~263 K and the boiling temperature of dodecane is 487–491 K. It has been justified that the TraPPE force field can well predict the melting points of alkanes, which were only slightly overestimated for C15 and C16 by ~16 and 15 K, respectively.[38,58] The range of temperatures, 310–410 K, under investigation in the present study is far away from the transition temperature of dodecane in bulk phase, indicating that the peculiar morphology of dodecane undergoing phase change is not because of melting or boiling but the interfacial crystallization due to its interaction with the silica substrate.

At 330 K, dodecane molecules spread over the substrate and alter the hemicylindrical droplet gradually to a thin film [0.1–2 ns in Fig. 6(a)], accompanied by the ordering of the attached layer due to the interfacial crystallization as P_{ee} increase to ~ −0.25. The stacks further reorganize and grow along the direction (z) normal to the substrate, as shown in Fig. 6(a) at 3 ns, and P_{ee} increases to a plateau value of −0.15. The final morphology in Fig. 6(a) at 5 ns features a well-organized thick lamellae structure covered by an amorphous rough free surface layer. The molecular end-to-end vector exhibits the preferential alignment with reference to the x axis [$P_{ee}(\theta_x) = 0.89$], and 79% of the molecules have an angle less than 15° referring to the x axis, as shown in Fig. 7(b). For molecules of the attached layer, it is 95% and $P_{ee}(\theta_x) = 0.96$.

It should be noted that there is almost no dodecane molecules in the nanopore, implying that there is no vapor phase of dodecane at temperatures lower than 330 K in S1. The phenomenon clearly indicates the interactions between dodecane and silica and among dodecane molecules are strong enough to stop dodecane
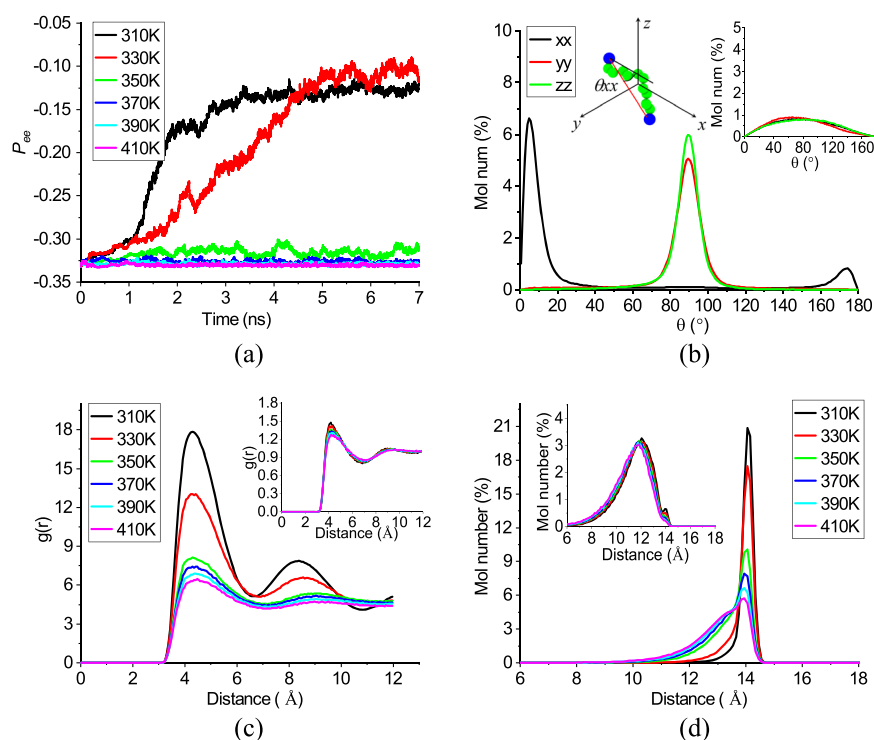
FIG. 7. Statistics of S1. Also given in 7b, 7c, and 7d are the corresponding profiles in bulk phase at 0.1 MPa. (a) Time evolution of the orientational order of dodecane molecules. (b) PDF of molecular orientation with reference to x, y and z axes. (c) RDF of dodecane –CH_3 group. (d) PDF of end-to-end intramolecular distance of dodecane.

molecules from escaping the substrate surface via evaporation at low temperatures.

It is therefore the competition between interfacial crystallization and surface wetting that largely determines the dodecane morphology in the nanopore. At 310 K, only a few dodecane molecules can spread over the substrate, generating a single layer, while the remaining are packed into distinct crystalline stacks parallel to the substrate [Fig. 6(b)]. This is because the interfacial crystallization dominates over the wetting, in addition to evaporation, and P_{ee} increases to a plateau in 3.5 ns, which is much faster than at 330 K, but with a smaller magnitude. The size of the solidified droplet at 310 K is ~13 nm in x direction, filled with seven consecutive stacks.

The dodecane morphology is sensitive to the system temperature. At 310 K, interfacial crystallization solely determines the dodecane morphology. At 330 K, interfacial crystallization and surface wetting play an equally important role. The dodecane molecules are spread over the substrate surface, forming a film. But the stacking still clearly exists in the film [Fig. 6(a) at 5 ns], with less layers compared to that at 310 K. With a further 20 K increase of the temperature at 350 K, as seen from Fig. 6(b), the orderly stacking largely disappears and the structuring on the contact layer appears as a faulty crystal. Figure 7(a) shows the orientational order of dodecane is much less than at 330 K. With further increase of the temperature, surface wetting dominates over interfacial crystallization, with dodecane molecules in film morphology and molecules in the contact layer disordered and randomly aligned without noticeable ordering at 370, 390 and 410 K. The respective $P_{ee}(\theta_x)$'s of the attached layers are 0.49, 0.43, and 0.40, which are close to the values in

bulk phase $[P_{ee}(\theta_x) = 0.33]$. Meanwhile, evaporation only becomes slightly stronger and is overall still weak, with countable dodecane molecules seen in the nanopore.

It should be mentioned that previous experimental studies reported a free film orientating normal to the substrate emerged on a frozen alkane droplet attached to a SiO_2 surface at temperatures above T_b (bulk freezing temperature).[59,60] It was attributed to the surface freezing at solid/vapor interfaces, as explained in the work of Merkl et al.[61] In a previous MD study performed in the work of Yamamoto et al.,[26] the metastable, ordered alkane monolayer (Langmuir-Blodgett film) at liquid-to-vapor interfaces at temperatures slightly above T_b appeared at a proper potential well of the substrate and film width. Experimental observations also confirmed the surface freezing process of long-chain alkanes on Mica surfaces,[34,62] which indicate that the collective dynamics of interfacial crystallization and surface freezing may occur in the adsorbed oil films when other caprocks are used as the substate. It should also be mentioned that the penetration of components with a higher polarity and the interfacial segregation effect of n-alkane mixtures should not be ignored when more practical crude oil mixtures are studied.[14,15,25,56] In Fig. 6, there is no surface freezing structure at liquid-to-vapor interface under all conditions with the number (1500) of dodecane molecules used in the present study.

2. Intermolecular and intramolecular distances

To provide further quantitative information on molecular structure and conformation to corroborate our previous statements, the temperature dependent RDF and end-to-end distance distribu-

tion in both S1 and bulk state are presented in Figs. 7(c) and 7(d). It should be noted that unlike the dodecane in bulk phase, the RDF magnitude in S1 deviates from physical values as the volume to compute the number density is not the vdW volume of the particles but the whole box. Despite this, it can still reflect the degree of crystallization within S1. The RDFs of the –CH$_3$ groups of dodecane in bulk phase agree well with experimental data, with the first prominent peak appearing at 4.2 Å.[63] There are two identifiable peaks, the second of which is not as prominent as the first one, and the first peak broadens slightly with the increase of temperature. In bulk phase, the peak magnitudes decrease gradually with the increase of temperature, and the RDFs in bulk phase approach 1 at long distances, which suggests that there is no long-range order in –CH$_3$ distribution. For the RDFs of dodecane in S1, the second peak can be clearly identified at 310 and 330 K, indicating the long-range ordered crystalline structures of –CH$_3$. The peak magnitude drops sharply when the temperature increases to 350 K, and the second peak almost disappears above 350 K, indicating that the dodecane molecules become more disordered and amorphous. The molecular chain length with the highest probability in bulk phase increases gradually from 12.21 to 12.38 Å as the temperature increases. Molecules in S1 are in stretched conformation, as the peak magnitudes are ~14 Å. At 310 and 330 K, 98% and 99% of dodecane molecules are longer than 13.5 and 14.5 Å, respectively. Even at temperatures above 350 K, dodecane molecules in S1 are much more stretched than in bulk phase. Like RDF, there is a sharp decrease of the peak magnitude when the temperature increases to 350 K.

3. Crystalline structures

To further quantify the layering of dodecane molecules in crystalline structures and the solid–liquid–vapor phase in Fig. 6, the temperature dependent density profile is plotted in Fig. 8(a). The dynamics of alkanes is dependent on the molecule conformation of the attached several layers above the substrate, as they determine the interfacial and viscous resistances.[64] The peak densities and the distances of the first three layers to the bottom boundary are plotted in Fig. 8(b).

TABLE III. The liquid/vapor densities and interfacial width, fitting density profile at $z > 35$ Å according to an error function.

T (K)	310	330	350	370	390	410
ρ_l (g/ml)	⋯	⋯	0.68	0.66	0.64	0.62
ρ_v (10^{-3} g/ml)	⋯	⋯	0.15	0.457	2.56	2.78
$\sqrt{2}w_\rho$ (Å)	⋯	⋯	4.75	5.97	6.24	6.83

The number of the identifiable layers seen from the density profile in Fig. 8(a) decreases with temperature increase. At 310 and 330 K, the density decays with oscillation as the z coordinate is further away from the substrate and drops sharply to zero at free surface, and there are stable plateaus representing a liquid phase at 350 K and above. The monotonically decreasing density profile of a liquid–vapor interface can be fitted by an error function (erf) as[65,66] $\rho(z) = 0.5(\rho_l + \rho_v) - 0.5(\rho_l - \rho_v)\,\text{erf}[(z - z_0)/(\sqrt{2}w_\rho)]$, where $\text{erf}(z) = 2/\sqrt{\pi}\int_0^z e^{-t^2}\,dt$. ρ_l and ρ_v are the densities of the liquid film and vapor gases, respectively. $\sqrt{2}w_\rho$ is the liquid-to-vapor interface width. The density of dodecane in liquid phase of S1 is ~ 5% lower than that in bulk phase at 350–410 K. Both the liquid-to-vapor interface width and vapor density increase with temperature (see Table III).

The cutoff distance of the LJ interaction is 12 Å without long-range tail correction, and the attractive force diminishes with the distance from the substrate out of the cutoff range. The density amplitude of the attached layer decreases steadily with the increasing temperature, while there is a turning point at 350 K in the 2nd and 3rd layers [Fig. 8(b)]. The abrupt change of the density peak has also been taken as a criterion to identify the phase transition in nanoconfined liquids.[67,68] The z_l's of different layers increase slightly and linearly with temperature, as shown in Fig. 8(b), and the gap between the 1st and 2nd layers remains almost constant with temperature, while it increases slightly between the 2nd and 3rd layers from 4.08 Å at 310 K to 4.65 Å at 410 K. This indicates that the average distance
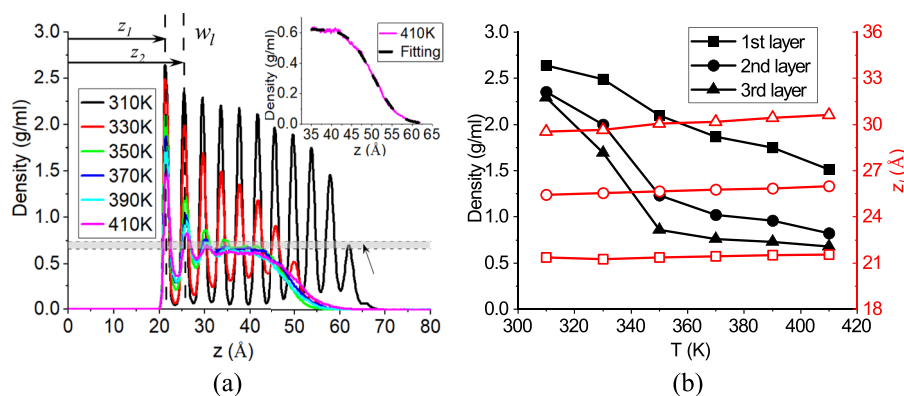

FIG. 8. Molecular structure and conformation in S1. (a) Density profiles of dodecane along the direction normal to the substrate. Statistics collected from the molecules located within the middle 30 Å in x direction, with a bin width of 0.1 Å in z direction. The inset indicates the fitting of the liquid-to-vapor density at 410 K. The density of dodecane in bulk phase at 0.1 MPa and 310–410 K is 0.66–0.74 g/ml, as indicated by the gray band bounded by dashed lines. (b) Effects of temperature on highest density and distance of the first three layers from the lower domain boundary.

between adjacent layers varies with the temperature and distance from the substrate, suggesting a need to revisit the effects of the varying layer gap on the interfacial and viscous resistances.[64]

B. Silica–H₂O–dodecane–silica system (S2)

1. H₂O–dodecane–silica interactions–interfacial crystallization vs competing water/dodecane wetting on silica

Since normal alkanes are strongly hydrophobic, and dodecane is immiscible with water over a wide range of temperatures and pressures,[69,70] there is no mechanism for dodecane to escape the silica surface in S2, as "evaporation" in S1. The dodecane morphology is therefore determined by the interactions between interfacial crystallization and competing wetting between water and dodecane on silica surface in S2.

Since water is a polar molecule, the electrostatic interaction can play a dominant role over vdW force[15] for its interaction with the silica surface. It has been proven that hydrogen bonding between water molecules and silanol groups can significantly enhance the wetting stability of water,[16,71,72] which would consequently impede the spreading of dodecane molecules over the substrate, i.e., water wetting wins against dodecane wetting. The electrostatic force induced hydrogen bonding has been found to be crucial in water flooded oil recovery, as it can help water molecules diffuse toward and approach the rock, thereby accelerating the detachment of oil droplets.[16,73] It can be inferred that the spreading of dodecane molecules over the silica surface will be "confined" by water wetting, which is referred to as the water confinement effects here.

It should be mentioned that both the quantity and lifetime of hydrogen bonds among water molecules and between water and Q2 decrease with the increase of temperature, resulting in the weakening of water confinement effects at elevated temperatures. This also accounts for the expansion of dodecane droplets and the broadening of contact lines in S2 [Fig. 9(c)] when the temperature increases.

2. Dodecane morphology and statistics

Snapshots of the dodecane droplet morphology in S2 are shown in Fig. 9. Generally, rock reservoirs are commonly categorized according to the contact angle (θ) as water wet ($105° \leq \theta \leq 180°$), oil wet ($0° \leq \theta \leq 75°$), or intermediate wet ($75° \leq \theta \leq 105°$) based on the competitive affinity of rock toward oil or water.[74] The contact angle of the sessile droplet of dodecane in S2 is determined by the density profile shown in Fig. 10 using[75] $(x - a)^2 + (z - b)^2 = R^2$ and $\theta = \cos^{-1}[(z_0 - b)/R]$, where a and b are the coordinates of the center of the fitted circle in x and z directions, respectively; R is the radius; z_0 is the height of the contact plane, which is set to be 50 Å at 310 K and 40 Å at other temperatures.[75] As shown in Fig. 10, Q2–silica tends to be water wet. The dodecane contact angle decreases from 130° at 310 K to ~100° when the temperature increases to 330 K and above.

The collective dynamics of interfacial crystallization and water confinement determines at 310–350 K the morphology of dodecane. At 310 and 330 K, the crystalline stacks can grow continuously until the dodecane–water interface. The droplet boundary deviates clearly from the fitted circle at 310 K in regions 3.0 nm above the substrate, where the dodecane molecules are packed in rectangular shape, similar to those in S1 [see Fig. 6(b)], but have a narrowed contact line.
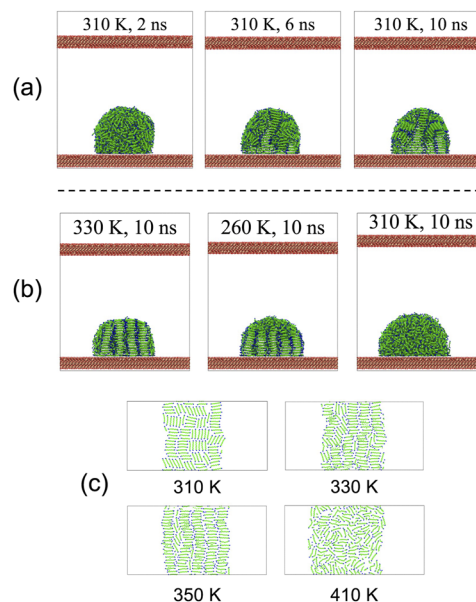

FIG. 9. (a) Time evolution of dodecane droplet in S2 at 310 K. H₂O molecules are hidden. (b) Dodecane morphology at 330, 350, and 410 K at 10 ns. (c) The layout of dodecane molecules of the contact layer at 310, 330, 350, and 410 K at 10 ns.

Water confinement can bend the stacks at 310 K in regions away from the substrate, while dodecane molecules are in well-organized lamellae structures at 330 K. Dodecane molecules in S2 have a much lower preferential orientation order both at 310 K [$P_{ee}(\theta_x) = 0.58$]
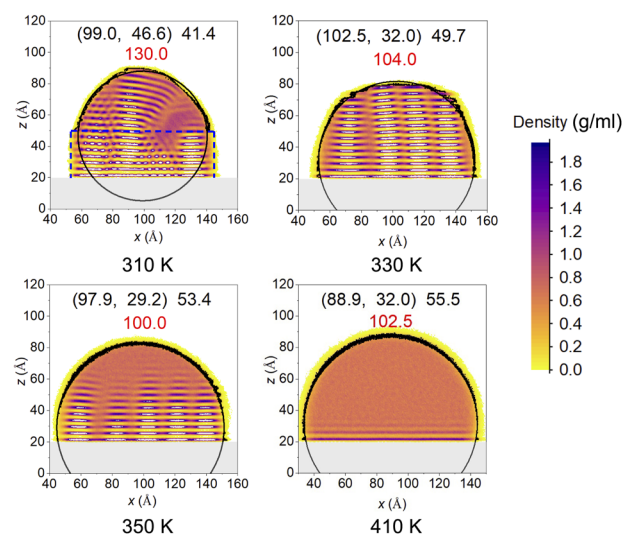

FIG. 10. 2D density contours of dodecane droplet at different temperatures in S2, averaged over the last 1 ns with the bin area equal to 0.5×0.5 Å × Å. The gray block indicates the silica substrate. The black dots indicate the data used for fitting the circle with the criterion $\rho = [0.2 - 0.5]$ g/ml.[76] The blue dashed box (9.5×3.0 nm × nm) is to highlight the droplet boundary. The black solid line indicates the fitted circle. The center coordinates (Å, Å), radius (Å) of the fitted circle, and the contact angle θ (°) are also indicated.

and 330 K $[P_{ee}(\theta_x) = 0.81]$ than in S1. Interfacial crystallization occurs at 350 K under the impact of the water confinement [see Fig. 6(b)], although there are still considerable dodecane molecules in liquid phase.

It is interesting to see that at 330 K, there exist four arrays on each of the stacks, with "melting" dodecane molecules "dripping" from the stack edge, as a chocolate fountain. While at 350 K, five arrays display on each stack, and those "melting" dodecane molecules appear on the top of the stack.

Compared with 310 and 330 K, dodecane molecules on the attached layer at 350 K have the finest alignment, with 91% of the molecules having an angle less than 15° between the principal and reference x axes $[P_{ee}(\theta_x) = 0.92]$.

At higher temperatures including 370, 390 and 410 K, the droplet morphology exhibits better circularity, and dodecane molecules are disordered on the attached layer without interfacial crystallization.

The quantified information on layering structure and dodecane molecule conformation in S2 is shown in Fig. 11. Similar to density profiles in S1, there are oscillatory decays of the density in the direction normal to and away from the substrate, except at 330 K between 30 and 60 Å. Only three layers in "solid" state can be identified from the density profiles at 370, 390, and 410 K, followed by a liquid phase with the densities being 0.71, 0.69, and 0.68 g/ml, respectively. The abrupt drop in density occurs in the 2nd and 3rd layers when the temperature increases to above 370 K. The dodecane molecules are generally closer to the substrate than in S1 as the distance of the peak densities away from the substrate is on average

0.62% shorter. There is no apparent variation of the layering gaps with temperature. Affected by water confinement, the structuring of dodecane molecules is more compact under all conditions. Both the RDF and PDF of the end-to-end intramolecular distance of dodecane at 330 K almost overlap with those at 310 K in S2. The RDF and PDF profiles at 350 K approach closer to those at 330 K in S2, while it is more similar to 370 K in S1. There is a clear second peak of RDF at 350 K in Fig. 11(c) because of the crystalline structure. The PDFs of dodecane in S2 present comparable profiles and peak values as in S1 at 310 K and 370–410 K. Water confinement affects the molecular conformation mainly at 330 and 350 K, as the peak values of PDFs increase by 12% and 40% than in S1 at 330 and 350 K, respectively. The molecule crystallization and stretchiness are greatly enhanced at 330 and 350 K.

C. Silica–CO₂–dodecane–silica system (S3)

1. CO₂-dodecane-silica interactions–dissolution vs competing CO₂/dodecane adsorption on silica

Time evolution of the dodecane droplet morphology in supercritical CO_2 is shown in Fig. 12. Unlike the confinement of dodecane molecules on silica surface in S2, dodecane dissolves into CO_2 under the conditions of 20 MPa and 310–410 K (the minimum miscibility pressure (MMP) of decane in 50-nm nanopore is ~4 to 7 MPa at 293–303 K.[77] More evidence from the diminishing interface method in MD simulation demonstrated that the MMPs in nanoslits of 2–16 nm are ~8 to 11 MPa[7]).
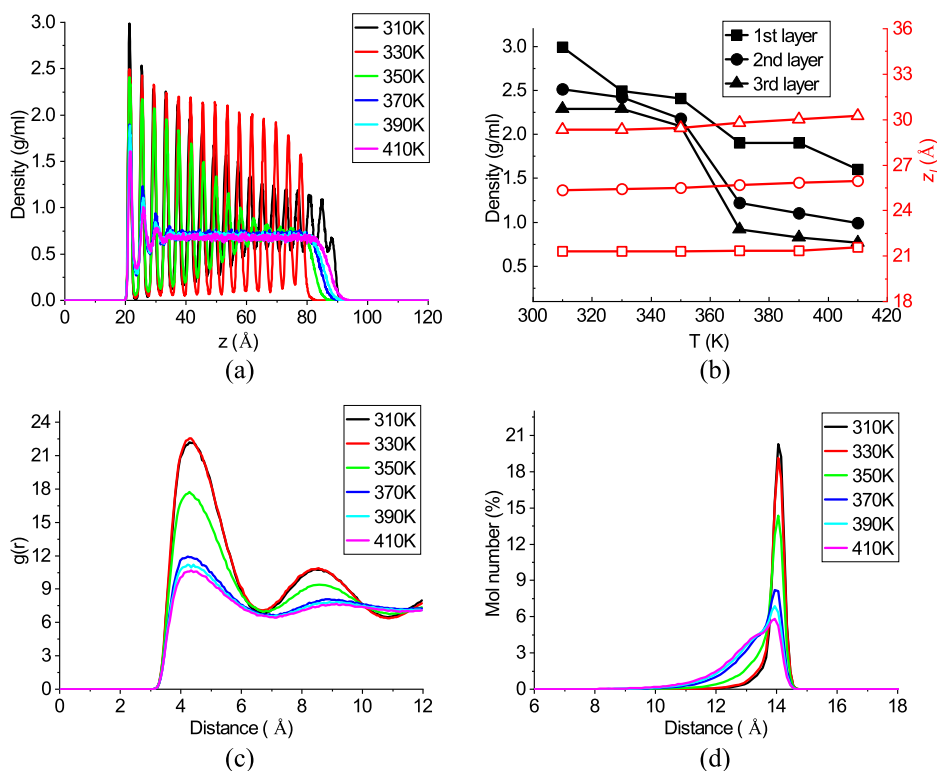

FIG. 11. Statistics in S2. (a) Density profiles of dodecane in z direction. (b) Temperature dependent peak densities and distance of the first three layers away from the bottom boundary. (c) RDF of dodecane molecules. (d) PDF of end-to-end distance of dodecane molecules.
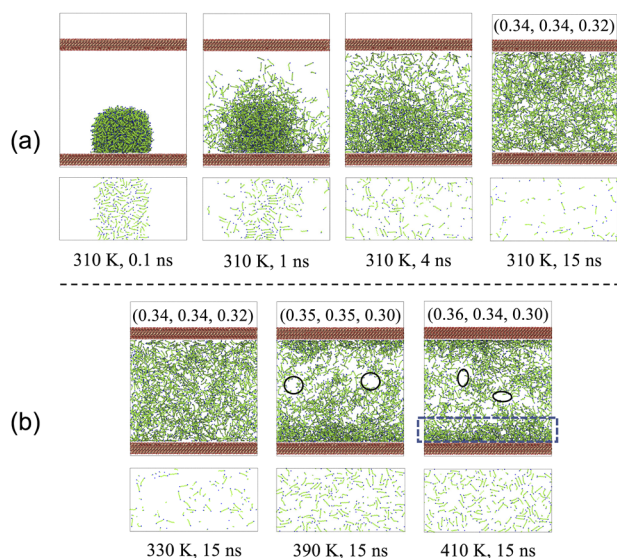
FIG. 12. (a) Time evolution of the dodecane morphology in S3 at 310 K and the corresponding snapshots of dodecane molecules on the attached layer at 1 Å above the surface of the bottom slab. (b) Dodecane molecule distribution at 15 ns at 330, 390, and 410 K. Voids and amorphous film are indicated. CO_2 molecules are hidden in all snapshots. $P_{ee}(\theta)$'s of x, y, and z directions are given in bracket.

The evolution of the droplet morphology in S3 is therefore the collective dynamics of dodecane dissolution in CO_2 and competing surface adsorption between CO_2 and dodecane. It can be seen from Fig. 12(a) that dodecane molecules dissolve rapidly into CO_2 (hidden for clarity) and the crystallized dodecane "droplet" at 0.1 ns disappears at 15 ns. It is clear that CO_2 working as an efficient solvent for the oil under typical undersurface conditions can be an important mechanism for CO_2 to reduce the thickness of the sticky layers and the hydrocarbon viscosity. The dissolution initiates in radial direction and the CO_2–dodecane interface gradually vanishes. Dodecane molecules reaching the top silica slab can be trapped and form an adsorption layer as shown in Fig. 12.

CO_2 is a nonpolar molecule and has a weaker affinity with Q2–silica surface than water. A CO_2–water–silica system is water wet since the contact angle of water is less than 50° at 318 K.[45] Here, in a CO_2–dodecane–silica system, during their dissolution in CO_2, dodecane molecules can also spread over the substrate under the impact of CO_2 adsorption, leading to an initial increase in dodecane molecules close to the substrates before 2 ns, as shown in Fig. 13(a). The number of molecules adsorbed on surface stabilizes in 2–8 ns. The concentration gradient in z direction drives dodecane molecules moving upward until the dissolution process fully completes at ~10 ns under all conditions.

There are two adsorption layers of dodecane and CO_2 under all conditions on both the bottom and top slabs, identified from
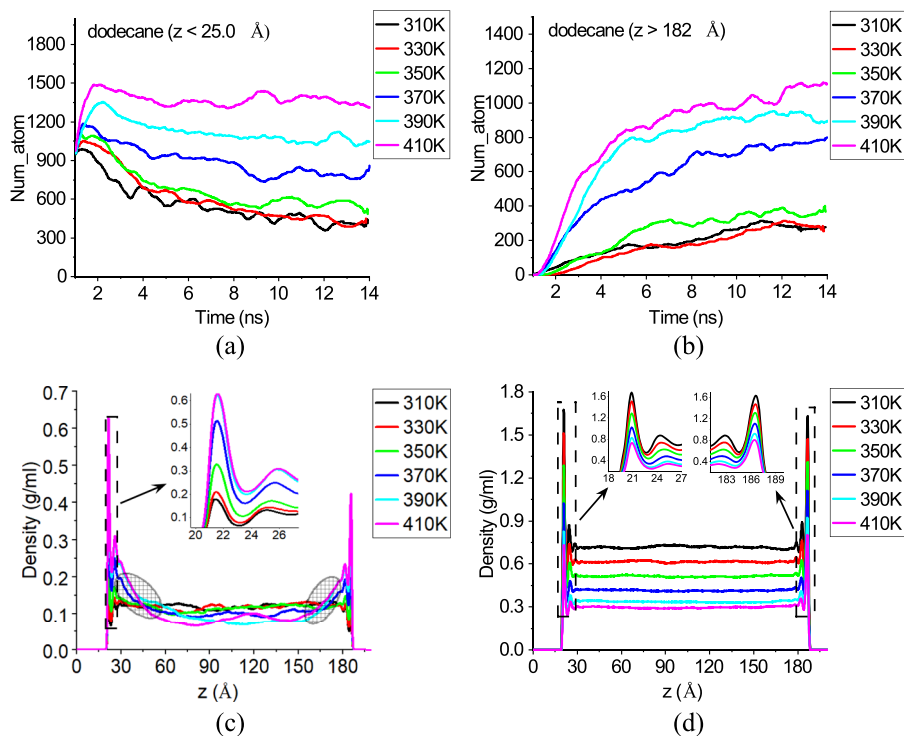

FIG. 13. Statistics of S3. In 13(a) and 13(b), time evolution of the number of dodecane molecules in specific regions in z direction is shown. The data are averaged over a 10 ps interval. In 13(c) and 13(d), density profiles in z direction at 15 ns are shown. The transition from surface adsorption to the free layer is highlighted in shadowed regions. (a) $z < 25$ Å. (b) $z > 182$ Å. (c) Dodecane. (d) CO_2.

the density profiles shown in Figs. 13(c) and 13(d). Unlike in S1, dodecane's densities at higher temperatures have a higher peak magnitude in S3, since more dodecane molecules are adsorbed on the slabs, as shown by the molecule distribution of the attached layer in Fig. 12.

The systems reach an equilibrium faster at higher temperatures, and finally dodecane molecules are randomly distributed in the nanoslits, with P_{ee} almost identical in three directions and close to those in bulk phase $[P_{ee}(\theta_x) = P_{ee}(\theta_y) = P_{ee}(\theta_z) = 0.33]$. In general, dodecane molecules are more uniformly distributed in S3 at lower temperatures as more CO_2 are deployed in the system (see Table I) and dissolution dominated mixing now plays the primary role.

Dodecane molecules of the adsorption layers on the bottom slab are more compact than those on the top slab at 370–410 K, and there is a transition region from the adsorption layer to the free layer where dodecane molecules aggregate to form an amorphous film of ~20 Å width with density varying in 0.1–0.2 g/ml. Randomly distributed voids in the nanoslit can be seen at 370–410 K in Fig. 12, which also accounts for the density fluctuation in the free layer in Fig. 13(c). The dodecane molecular distribution also alters the CO_2 density profile in Fig. 13(d), as compared with Fig. 5(d). CO_2 molecules are uniformly distributed in the free layer under all conditions, and the density of the first adsorption layer on the top slab is ~ 1.1 times that on the bottom one at 350–410 K.

IV. CONCLUSIONS

The interfacial crystallization of dodecane on hydroxylated silica at 310–410 K is studied using molecular dynamics simulation in a nanopore of dodecane–silica (S1). Two systems other, i.e., silica–H_2O-dodecane–silica (S2) and silica–CO_2-dodecane–silica (S3), are built to model the impact of water and CO_2 on interfacial crystallization of dodecane on silica surface. Two methodologies on how to control the pressure of liquids efficiently and effectively in nanoslits are investigated. The morphology of the dodecane droplet, layering stacks of the crystalline structures, and molecular conformation are quantified and investigated. The conclusions are drawn as follows:

The crystalline stacks exist at 310 and 330 K but are organized in two different morphologies, i.e., a frozen droplet and a lamellae film, respectively. Dodecane molecules have the best in-plane preferential orientation at 330 K. At 350 K and above, a film of dodecane emerges, with multiple solid, liquid, and vapor phases coexisting and a few diffusing dodecane molecules in the nanoslit. The density of the attached layers can be 2–5 times higher than that of the liquid bulk phase. Increase in temperature reduces the crystallization, stretchiness, and layering gaps of dodecane.

S2 is water wet because of the strong hydrogen bonding interaction between water molecules and the silanol groups, which impedes the spreading of dodecane molecules over the substrate. Dodecane molecules exist in droplet morphology, with structures changing with temperatures. The lamellae structures show up in S2 at 350 K and have the finest preferential orientation of the contact layer. Water confinement deforms the circularity of the dodecane droplet at 310–330 K. Water confinement increases the crystalline order and stretchiness of dodecane molecules and narrows the layering gaps.

Dodecane droplets are dissolved in supercritical CO_2 of 20 MPa in S3, generating a nano-confined CO_2–dodecane mixture. Both dodecane and CO_2 molecules are nonuniformly distributed in nano-confined direction, consisting of the adsorption layers on substrates and free layers in the middle region. CO_2 and dodecane are better mixed at 310 and 330 K, as a higher density of CO_2 in the system enhances the dissolution.

Overall, the dodecane morphology under typical depleted reservoir conditions is determined by the interactions between interfacial crystallization and surface adsorption (or wetting). Depending on the system configuration, there can exist a third mechanism that accounts for the escape of dodecane molecules from the silica surface, as "evaporation" in S1 or dissolution in S3, which can become the dominant physics affecting the dodecane morphology and mobility, as we have seen in S3 that CO_2 is an efficient solvent for dodecane under typical undersurface conditions. Since water will form a film over the hydrophilic rock surface and detach the remaining oil from the surface, the recovered oil is to be transported by water in "liquid droplet" morphology since it is immiscible with water. On the other hand, since oil dissolves in supercritical CO_2, it will be transported by CO_2 more like a solute in a solution. Comparing detachment with dissolution, it can be inferred that CO_2 is advantageous for recovering oil from depleted oil reservoirs in regard to time and effort, as has been practiced in oil recovery engineering, i.e., using the tertiary CO_2 enhanced oil recovery following secondary water flooding.

SUPPLEMENTARY MATERIAL

See the supplementary material for force fields, their key parameters, and validation on CO_2 and H_2O densities in bulk phase.

AUTHOR DECLARATIONS

Conflict of Interest

The authors have no conflicts to disclose.

Author Contributions

Cheng Chen: Conceptualization (equal); Data curation (lead); Formal analysis (lead); Investigation (lead); Methodology (lead); Project administration (supporting); Resources (equal); Software (lead); Validation (lead); Visualization (lead); Writing – original draft (lead); Writing – review & editing (supporting). **Jun Xia**: Conceptualization (equal); Funding acquisition (supporting); Methodology (supporting); Project administration (equal); Resources (equal); Supervision (lead); Visualization (supporting); Writing – original draft (supporting); Writing – review & editing (lead). **Quentin**

Martinez: Formal analysis (supporting); Methodology (supporting). **Xi Jiang**: Resources (supporting); Writing – review & editing (supporting). **Hamid Bahai**: Funding acquisition (lead); Project administration (equal); Resources (supporting); Writing – review & editing (supporting).

DATA AVAILABILITY

REFERENCES

[1] B. Hill, S. Hovorka, and S. Melzer, "GHGT-11, Energy Procedia," in International Conference on Greenhouse Gas Technologies (GHGT), Kyoto, Japan, 18–22 November, 2012, edited by T. Dixon and K. Yamaji (Elsevier Science BV, Amsterdam, The Netherlands, 2013), Vol. 37, pp. 6808–6830.

[2] H. Yu, H. Xu, J. Fan, Y.-B. Zhu, F. Wang, and H. Wu, Energy Fuels **35**, 911 (2021).

[3] K. Wu, Z. Chen, J. Li, X. Li, J. Xu, and X. Dong, Proc. Natl. Acad. Sci. U. S. A. **114**, 3358 (2017).

[4] T. A. Ho, D. V. Papavassiliou, L. L. Lee, and A. Striolo, Proc. Natl. Acad. Sci. U. S. A. **108**, 16170 (2011).

[5] J.-L. Barrat and L. Bocquet, Phys. Rev. Lett. **82**, 4671 (1999).

[6] D. M. Huang, C. Sendner, D. Horinek, R. R. Netz, and L. Bocquet, Phys. Rev. Lett. **101**, 226101 (2008).

[7] T. Fang, Y. Zhang, J. Liu, B. Ding, Y. Yan, and J. Zhang, Int. J. Heat Mass Transfer **141**, 643 (2019).

[8] X. Li, P. Wang, Z. Yan, S. Yu, K. Wei, X. Zhu, Y. Sun, and Q. Xue, Chem. Eng. J. **431**, 133988 (2022).

[9] K. Zhang, N. Jia, S. Li, and L. Liu, Chem. Eng. J. **351**, 1115 (2018).

[10] K. Wu, X. Li, C. Wang, W. Yu, and Z. Chen, Ind. Eng. Chem. Res. **54**, 3225 (2015).

[11] G. J. Wang and N. G. Hadjiconstantinou, Langmuir **34**, 6976 (2018).

[12] Z. Sun, B. Huang, S. Yan, S. Wang, K. Wu, W. Yu, Y. Li, and S. Wang, Ind. Eng. Chem. Res. **61**, 4971 (2022).

[13] K. Ghosh and C. V. Krishnamurthy, Phys. Rev. E **97**, 012131 (2018).

[14] M. Ahmadi and Z. Chen, Energy **254**, 124434 (2022).

[15] J. Zhong, P. Wang, Y. Zhang, Y. Yan, S. Hu, and J. Zhang, Energy **59**, 295 (2013).

[16] J. Tang, Z. Qu, J. Luo, L. He, P. Wang, P. Zhang, X. Tang, Y. Pei, B. Ding, B. Peng, and Y. Huang, J. Phys. Chem. B **122**, 1905 (2018).

[17] Z. Cao, H. Jiang, J. Zeng, H. Saibi, T. Lu, X. Xie, Y. Zhang, G. Zhou, K. Wu, and J. Guo, Chem. Eng. J. **420**, 127578 (2021).

[18] Y. Yang, A. K. Narayanan Nair, M. F. A. Che Ruslan, and S. Sun, Fuel **310**, 122332 (2022).

[19] S. Tian, V. Erastova, S. Lu, H. C. Greenwell, T. R. Underwood, H. Xue, F. Zeng, G. Chen, C. Wu, and R. Zhao, Energy Fuels **32**, 1155 (2018).

[20] S. Wang, Y. Liang, Q. Feng, and F. Javadpour, Fuel **310**, 122480 (2022).

[21] D. Feng, Z. Chen, K. Wu, J. Li, Y. Gao, J. Bi, S. Zhang, and F. Peng, Fuel **327**, 125128 (2022).

[22] G. T. Chala, S. A. Sulaiman, and A. Japper-Jaafar, J. Non-Newtonian Fluid Mech. **251**, 69 (2018).

[23] J. Wang, Y. Hao, B. Zhu, T. Han, Z. Li, and J. Zhang, J. Phys. Chem. B **126**, 985 (2022).

[24] Y. Gan, Q. Cheng, S. Chu, Z. Wang, G. Luan, W. Sun, S. Wang, C. Liu, Q. Li, and Y. Liu, Energy Fuels **35**, 4012 (2021).

[25] T. Yamamoto, Polymer **99**, 721 (2016).

[26] T. Yamamoto, K. Nozaki, A. Yamaguchi, and N. Urakami, J. Chem. Phys. **127**, 154704 (2007).

[27] A. J. Bourque, C. R. Locker, and G. C. Rutledge, J. Phys. Chem. B **121**, 904 (2017).

[28] Y. Gong, W. Zhang, and R. G. Larson, Macromolecules **55**, 6311 (2022).

[29] Z. Wu, S. N. Ehrlich, B. Matthies, K. W. Herwig, P. Dai, U. G. Volkmann, F. Y. Hansen, and H. Taub, Chem. Phys. Lett. **348**, 168 (2001).

[30] A. J. Bourque and G. C. Rutledge, Eur. Polym. J. **104**, 64 (2018).

[31] X. Gao, P. Huber, Y. Su, W. Zhao, and D. Wang, J. Phys. Chem. B **120**, 7522 (2016).

[32] C. Wang, L. Gao, M. Liu, S. Xia, and Y. Han, Chem. Eng. J. **452**, 139287 (2023).

[33] J. Gao, W. D. Luedtke, and U. Landman, Phys. Rev. Lett. **79**, 705 (1997).

[34] N. Maeda, M. M. Kohonen, and H. K. Christenson, J. Phys. Chem. B **105**, 5906 (2001).

[35] S. T. Cui, P. T. Cummings, and H. D. Cochran, J. Chem. Phys. **114**, 7189 (2001).

[36] A. Jabbarzadeh, P. Harrowell, and R. I. Tanner, Phys. Rev. Lett. **96**, 206102 (2006).

[37] A. Jabbarzadeh, P. Harrowell, and R. I. Tanner, Phys. Rev. Lett. **94**, 126103 (2005).

[38] S. A. Burrows, I. Korotkin, S. K. Smoukov, E. Boek, and S. Karabasov, J. Phys. Chem. B **125**, 5145 (2021).

[39] C. Chen, D. Mira, and X. Jiang, Fuel **316**, 123356 (2022).

[40] H. Wang, L. Chen, Z. Qu, Y. Yin, Q. Kang, B. Yu, and W.-Q. Tao, Appl. Energy **262**, 114575 (2020).

[41] Y. Tan, Q. Li, L. Xu, A. Ghaffar, X. Zhou, and P. Li, Fuel **328**, 125256 (2022).

[42] J. T. Tetteh, P. V. Brady, and R. Barati Ghahfarokhi, Adv. Colloid Interface Sci. **284**, 102253 (2020).

[43] H. Heinz, T.-J. Lin, R. Kishore Mishra, and F. S. Emami, Langmuir **29**, 1754 (2013).

[44] C. Chen, N. Zhang, W. Li, and Y. Song, Environ. Sci. Technol. **49**, 14680 (2015).

[45] C. Chen, B. Dong, N. Zhang, W. Li, and Y. Song, Energy Fuels **30**, 5027 (2016).

[46] J. J. Potoff and J. I. Siepmann, AIChE J. **47**, 1676 (2001).

[47] C. G. Aimoli, E. J. Maginn, and C. R. A. Abreu, J. Chem. Phys. **141**, 134101 (2014).

[48] S. Plimpton, J. Comput. Phys. **117**, 1 (1995).

[49] A. Stukowski, Modell. Simul. Mater. Sci. Eng. **18**, 015012 (2010).

[50] Y. Zhao, W. Li, S. Zhan, and Z. Jin, Phys. Chem. Chem. Phys. **24**, 17195 (2022).

[51] C. M. Tenney and R. T. Cygan, Environ. Sci. Technol. **48**, 2035 (2014).

[52] J. Zhou, J. Zhang, J. Yang, Z. Jin, and K. H. Luo, Chem. Eng. J. **428**, 132020 (2022).

[53] W. G. Hoover, Phys. Rev. A **31**, 1695 (1985).

[54] H. J. C. Berendsen, J. P. M. Postma, W. F. van Gunsteren, A. Dinola, and J. R. Haak, J. Chem. Phys. **81**, 3684 (1984).

[55] R. S. M. Freitas, Á. P. F. Lima, C. Chen, F. A. Rochinha, D. Mira, and X. Jiang, Fuel **329**, 125415 (2022).

[56] S. Math, J. Gao, and U. Landman, J. Phys. Chem. C **126**, 4209 (2022).

[57] X. Tong, P. Yang, M. Zeng, and Q. Wang, Langmuir **36**, 8422 (2020).

[58] L. Dai, P. P. Rutkevych, S. Chakraborty, G. Wu, J. Ye, Y. H. Lau, H. Ramanarayan, and D. T. Wu, Phys. Chem. Chem. Phys. **23**, 21262 (2021).

[59] H. Schollmeyer, B. Ocko, and H. Riegler, Langmuir **18**, 4351 (2002).

[60] H. Schollmeyer, B. Struth, and H. Riegler, Langmuir **19**, 5042 (2003).

[61] C. Merkl, T. Pfohl, and H. Riegler, Phys. Rev. Lett. **79**, 4625 (1997).

[62] N. Maeda, M. M. Kohonen, and H. K. Christenson, Phys. Rev. E **61**, 7239 (2000).

[63] G. E. Lindberg, J. L. Baker, J. Hanley, W. M. Grundy, and C. King, Liquids **1**, 47 (2021).

[64] K. Wu, Z. Chen, J. Li, Z. Lei, J. Xu, K. Wang, R. Li, X. Dong, S. Yang, F. Zhang, Z. Chen, and Y. Gao, J. Phys. Chem. C **123**, 16456 (2019).

[65] T. K. Xia and U. Landman, J. Chem. Phys. **101**, 2498 (1994).

[66] T. K. Xia, J. Ouyang, M. W. Ribarsky, and U. Landman, Phys. Rev. Lett. **69**, 1967 (1992).

[67] S. Han, M. Y. Choi, P. Kumar, and H. E. Stanley, Nat. Phys. **6**, 685 (2010).

[68] H. Qiu and W. Guo, J. Phys. Chem. Lett. **10**, 6316 (2019).

[69] B. Liu, J. Shi, M. Wang, J. Zhang, B. Sun, Y. Shen, and X. Sun, J. Supercrit. Fluids **111**, 171 (2016).

[70] P. Morgado, J. Barras, P. Duarte, and E. J. M. Filipe, Fluid Phase Equilib. **503**, 112322 (2020).

[71] F. S. Emami, V. Puddu, R. J. Berry, V. Varshney, S. V. Patwardhan, C. C. Perry, and H. Heinz, Chem. Mat. **26**, 2647 (2014).

[72] Y. Dou, Q. Bai, K. Yang, W. Guo, H. Wang, and S. Chen, J. Mol. Liq. **366**, 120268 (2022).

[73] Q. Liu, S. Yuan, H. Yan, and X. Zhao, J. Phys. Chem. B **116**, 2867 (2012).

[74] S. Iglauer, C. H. Pentland, and A. Busch, Water Resour. Res. **51**, 729, https://doi.org/10.1002/2014wr015553 (2015).

[75] H. Jiang and A. J. Patel, Curr. Opin. Chem. Eng. **23**, 130 (2019).

[76] F. Jiménez-Ángeles and A. Firoozabadi, J. Phys. Chem. C **120**, 11910 (2016).

[77] B. Bao, J. Feng, J. Qiu, and S. Zhao, ACS Omega **6**, 943 (2021).

07 October 2023 12:30:18